International Journal of Bioprinting

RESEARCH ARTICLE

An integrated *in silico–in vitro* approach for bioprinting core–shell bioarchitectures

Nicole Guazzelli[1,2,3†], Ludovica Cacopardo[1,2,3†*], Alessandro Corti[4], Arti Ahluwalia[1,2,3]

[1]Department of Information Engineering, University of Pisa, Pisa, Italy

[2]Research Center E. Piaggio, University of Pisa, Pisa, Italy

[3]3R Centre, Inter-University Centre for the Promotion of the 3R Principles in Education and Research, University of Pisa, Pisa, Italy

[4]Department of Translational Research and New Technologies in Medicine and Surgery, University of Pisa, Pisa, Italy

(This article belongs to the *Special Issue: 3D Bioprinting for Materials and Application*)

Abstract

Biological tissues possess a high degree of structural complexity characterized by curvature and stratification of different tissue layers. Despite recent advances in *in vitro* technology, current engineering solutions do not comprise both of these features. In this paper, we present an integrated *in silico–in vitro* strategy for the design and fabrication of biological barriers with controlled curvature and architecture. Analytical and computational tools combined with advanced bioprinting methods are employed to optimize living inks for bioprinting-structured core–shell constructs based on alginate. A finite element model is used to compute the hindered diffusion and crosslinking phenomena involved in the formation of core–shell structures and to predict the width of the shell as a function of material parameters. Constructs with a solid alginate-based shell and a solid, liquid, or air core can be reproducibly printed using the workflow. As a proof of concept, epithelial cells and fibroblasts were bioprinted respectively in a liquid core (10 mg/mL Pluronic) and in a solid shell (20 mg/mL alginate plus 20 mg/mL gelatin, used for providing the cells with adhesive moieties). These constructs had a roundness of 97.6% and an average diameter of 1500 ±136 μm. Moreover, their viability was close to monolayer controls (74.12% ± 22.07%) after a week in culture, and the paracellular transport was twice that of cell-free constructs, indicating cell polarization.

Keywords: Core–shell spheroids; Bioprinting; 3D models; Curvotaxis; Biological barriers; *In silico* models

†These authors contributed equally to this work.

***Corresponding author:**
Ludovica Cacopardo
(ludovica.cacopardo@unipi.it)

Citation: Guazzelli N, Cacopardo L, Corti A, *et al*., 2023, An integrated *in silico–in vitro* approach for bioprinting core–shell bioarchitectures. *Int J Bioprint,* 9(5): 771.
https://doi.org/10.18063/ijb.771

Received: March 4, 2023
Accepted: May 2, 2023
Published Online: June 12, 2023

1. Introduction

Many organs possess a multilayer organization which derives from tissue primordia[1,2]. *In vivo*, the tissue layers form complex three-dimensional (3D) shapes which may often be topologically represented by core–shell structures. Cell constructs with core–shell geometries can be fabricated to recapitulate these architectures and are a fascinating research topic. They also provide a means of investigating cell organization in highly

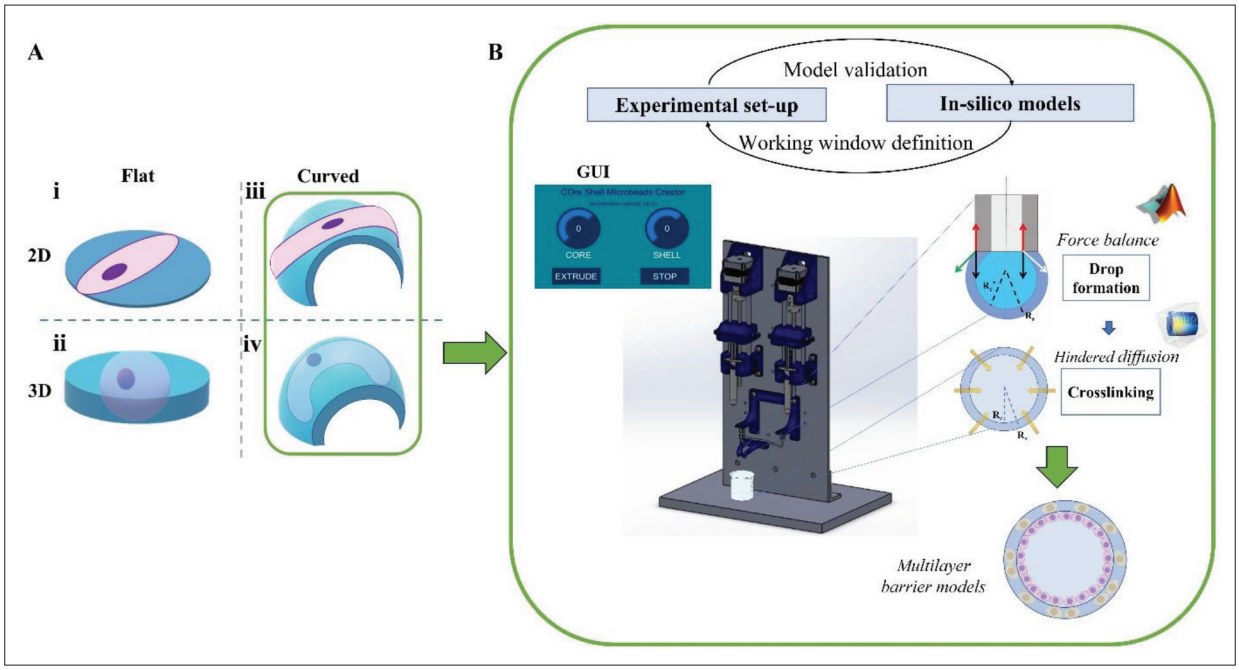

Figure 1. (A) Cell morphology in relation to substrate shape and dimensionality: (i) on 2D planar substrates, cells are typically flattened and highly spread; (ii) on 2D curved surfaces, cell bodies follow the substrate shape but maintain a flat aspect; (iii) on 3D planar substrates, cells assume rounder shapes with a lower surface-to-volume ratio; (iv) in the 3D curved conditions typical of *in vivo* tissues, the low surface-to-volume ratio is combined with a curved shape. (B) Workflow for the fabrication of CSCs replicating 2D and 3D curved substrates.

controlled conditions, considering both construct geometry and culture environment.

Biological barriers, such as the intestinal and alveolar barrier, are examples of tissues which can be recapitulated by core–shell structures. However, to date, *in vitro* barrier models are mainly based on flat two-dimensional (2D) culture systems in static or dynamic conditions. Transwells, composed of a semipermeable membrane which is able to separate the apical and basal compartments, represent the standard for barrier models. They can be used to mimic liquid–liquid (e.g., intestinal barrier) or air–liquid interfaces (e.g., lung barrier). A plethora of bioreactors of different shapes and sizes can also be found in the literature. These systems can apply dual-flow conditions or mechanical stimuli on cells cultured on flat, 2D membranes. Although the application of flow results in a more physiological environment with respect to static culture, the lack of a 3D architecture is likely to affect cell phenotype, and consequently, the translational value of results may be compromised[3-6]. To address this issue, some examples of 3D barrier models—in which cells are embedded within a gel-like (solid) medium or biomaterial which mimics the mechanical and biochemical features of the native extracellular matrix (ECM)—have been reported. However, the models fail in reproducing the curvature of native tissues, which is also known to be an important cue in directing cell behavior [3,7,8]. Indeed, the curvature and dimensionality of culture substrates are known to affect the formation of actin fibers and the localization of focal adhesions, actomyosin contractility, differentiation, or cell morphology as depicted in Figure 1A[9,10].

A promising technology to achieve physiologically relevant 3D curvatures is through the generation of spheroids and organoids[6,8,11]. Endoderm-derived cells, such as lung or intestinal cells, have the peculiar capacity to form lumens, a capacity likely related to collective cell polarization[12]. Recent studies report the spontaneous formation of intestinal and alveolar spheroids with a central lumen encapsulating primary cells or cell lines such as human colon carcinoma (Caco-2) cells or pulmonary adenocarcinoma (A549) in Matrigel. The diameter of the structures was around 50–120 μm, and their formation occurred between 7 and 21 days[13,14]. Organoids were also generated from biopsies or combining primary cells and pluripotent stem cells, with preparation times ranging from 3 to more than 4 weeks. Notably, the lumen formed in intestinal organoids often presents positive and negative curvatures similar to the intestinal crypts observed *in vivo*[15-17].

Although organoids have important advantages in terms of cell organization and differentiation, they do possess critical drawbacks, which may limit their application in regulatory or off-the-shelf applications

and hinder their scale-up; they are time-consuming and expensive to generate and maintain. Moreover, they suffer from a lack of reproducibility which is in part intrinsic to the self-assembly process and to the fact that protocols vary from laboratory to laboratory[18,19].

The bioprinting of structured core–shell constructs (CSCs) using standardized cell lines can be an optimal solution to overcome these limitations, as it enables the generation of curved 3D structures which can be controlled in terms of material composition, size, and lumen/external diameter ratio[20]. Bioprinting is a process based on 3D printing techniques that exploits the combination of cells, adhesion factors, and biomaterials to produce constructs for mimicking the characteristics of a tissue and includes a wide range of techniques based on droplet or filament extrusion and deposition[21]. Cell-laden drops or filaments constitute simple 3D structures that are further crosslinked to maintain their shape, while more complex architectures can be obtained by layer-by-layer deposition. Several fabrication strategies in the literature are almost exclusively based on the use of alginate which undergoes rapid gelation in contact with divalent cations[22]. Techniques range from coaxial electro-dropping to microfluidic and in air-microfluidics with applications in drug delivery, drug release, and therapy and tissue engineering[23–26]. For instance, a flow focusing microfluidic device was used to encapsulate a soft cell-collagen core in an alginate shell. The solutions were extruded in a continuous oil flow containing Ca^{2+} ions, allowing shell gelation and the formation of CSCs with an average diameter of 380 μm[27]. Gelatin methacrylate (GelMA) has also been used to encapsulate cells in a methyl cellulose core. The polymers were extruded in oil, and the GelMA shell was crosslinked by ultraviolet (UV) radiation, obtaining core–shell microgels with diameters of around 278 μm[28].

Some of these strategies are equipment-intensive, and the majority are limited in terms of their dynamic range and compatibility with cell encapsulation. The novelty of our approach is the integration of computational methods with coaxial bioprinting strategies for the fabrication of structured luminal bioarchitectures using a variety of cell-compatible materials. This enables the *a priori* definition of a working window, thus minimizing experimental time and cost. Here, we describe the integrated workflow, exploiting the COre-Shell MIcrobead Creator (COSMIC), which was designed for bioprinting cell-incorporated CSCs in a repeatable manner and with a wide range of materials (Figure 1B), resulting in a variety of structures with solid shells and either solid, liquid, or air-filled cores, capable of replicating different biological interfaces. As a proof of concept, a core–shell multilayer barrier model with alveolar epithelial cells and fibroblasts was generated[29].

2. Materials and methods

Alginate, a widely used material in bioprinting[21], was used as the base material for its biocompatibility and rapid physical gelation after extrusion was used as the base material for its biocompatibility, mildness, and fast gelation after extrusion. Other materials considered in our models and experiments were air, water, and Pluronic. The material properties and core–shell materials combinations analyzed are reported (**Section S1** in Supplementary File). In this study, we used two commercial coaxial needles (Ramé-hart Instrument Co., USA): needle 1 with an inner diameter (ID) = 26 Gauge (0.254 mm) and an outer diameter (OD) = 19 Gauge (0.69 mm), and needle 2 with the same ID and an OD = 16 Gauge (1.19 mm).

2.1. *In silico* modeling of the CSCs fabrication

In the *in silico* workflow, the initial shell and core extruded drop radii (R_s and R_c^*) were estimated as a function of the extrusion flow rates and material properties (surface tension γ and dynamic viscosity μ) by numerically solving the surface tension–gravity–flow force balance equation (detailed in **Section S2** in Supplementary File). Despite the complex nature of the hydrodynamic problem[29], this simplified approach enabled the estimation of initial R_s and R_c^*, minimizing the computational cost. Surface tension was measured with a tensiometer (Optics Theta Lite, Biolin Scientific, Sweden) using the pendant drop test, while dynamic viscosity was characterized using a viscosimeter (Brookfield DV-II+ Pro, AMETEK Brookfield, Germany) equipped with an LV1 spindle, at 37°C (see **Section S2** and **Tables S1** and **S2** in Supplementary File), at a shear rate of 1.3×10^3 s^{-1}.

The radii derived for each combination of core and shell materials were used as initial values to define the geometry of an axial symmetric finite element method (FEM) model implemented in Comsol Multiphysics 6, solving the reaction–diffusion equations for the transport of diluted species (Ca^{2+} ions) from an external fluid domain to porous media domains representing the alginate shell and core, respectively. The formation of G-blocks during Ca^{2+}-mediated alginate crosslinking (Equation I) was implemented as a second-order reaction since it depends on both the concentration of Ca^{2+} ions and the concentration of non-crosslinked alginate[30,31].

$$\frac{d\alpha}{dt} = k\frac{c_{Ca2+}}{c_{Alg0}}(1-\alpha) \quad \text{(I)}$$

Where k is the reaction rate of the gelation, $c_{Ca^{2+}}$ is the concentration of Ca^{2+} and c_{Alg_0} is the initial concentration of un-crosslinked alginate[30,31]. An apparent diffusion coefficient

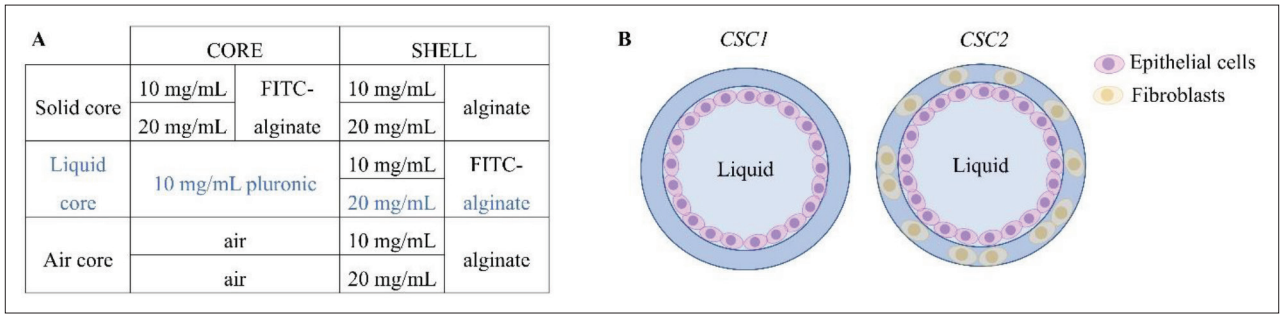

A	CORE		SHELL	
Solid core	10 mg/mL	FITC-alginate	10 mg/mL	alginate
	20 mg/mL		20 mg/mL	
Liquid core	10 mg/mL pluronic		10 mg/mL	FITC-alginate
			20 mg/mL	
Air core	air		10 mg/mL	alginate
	air		20 mg/mL	

Figure 2. (A) Selected material combinations for the experimental CSCs characterization. The condition tested in the presence of cells is highlighted in blue. (B) Schematic of the cellular models investigated as a preliminary proof of concept.

D_{app} (Equation II) was introduced to couple reaction–diffusion and crosslinking phenomena:

$$D_{app}(t) = abD_0 \tag{II}$$

where:

$$D_0 = \frac{k_b T}{6\pi\mu R_H} \tag{III}$$

$$a = 1 + (\delta - 1)\frac{e^{\left(-\frac{n\alpha(t)}{\alpha^*}\right)} - 1}{e^{\left(-\frac{n}{\alpha^*}\right)} - 1} \tag{IV}$$

$$b = \left\{1 + \left(\frac{R_H^{\,2}}{\kappa(\alpha(t))}\right)^{\frac{1}{2}} + \frac{1}{3}\left(\frac{R_H^{\,2}}{\kappa(\alpha(t))}\right)\right\}^{-1} \tag{V}$$

D_0 (Equation III) represents the value of the free diffusion coefficient, controlled by the size of the macromolecule as described by the Einstein–Stokes equation, where k_b is Boltzmann's constant, T the temperature in Kelvin, μ the solvent viscosity, and R_H is the hydrodynamic radius. a (Equation IV) represents the time-dependent coefficient that considers the effect of the degree of gelation α, defined as the ratio between the calcium- and time-dependent concentration of crosslinked alginate and the initial concentration of free alginate[30,31] and b (Equation V) is the Brinkmann coefficient which considers the influence of hindered diffusion in the spherical gel structure[32]. $\kappa(\alpha)$ represents the permeability of the structure as a function of α. **Section S3** (Supplementary File) details how b and κ were estimated on the basis of the Brinkmann and Carman–Kozeny equations[32]. The values for α^* (gelation value corresponding to the liquid-like to solid-like transition), δ (diffusion coefficient ratio before and after the crosslinking process), n (model parameter governing the rate of diffusivity change[31]) and R_H were adapted from the literature and optimized on the basis of the experimental results performing least-square minimization (see **Section S3** and **Table S6** in Supplementary File).

A time-dependent study (see **Section S4** in Supplementary File for more details on the numerical algorithm adopted) was used to consider different crosslinking times and obtain the concentrations of un-crosslinked and crosslinked alginate gel and calcium ions diffusing within the structure. The final core radius after the crosslinking process (R_c, VI) was derived as the radius corresponding to C_{gel} for which α is below α^*.

$$R_c = r\big|_{\alpha<\alpha^*} \tag{VI}$$

Finally, the shell thickness was computed as the difference between the R_s (estimated from drop formation theory) and the R_c. These results were used to define the experimental working window on the basis of crosslinking times, material properties, and extrusion parameters.

2.2. Experimental fabrication and characterization of the CSCs

The *in silico* results were used to identify the material and extrusion conditions (reported in Figure 2A), which guarantee an optimal structure in terms of distinction of core and shell and roundness. All solutions were prepared in deionized water. In particular, alginate (A0682, average molecular weight 12–80 kDa, R_h 200 nm, Sigma Aldrich) was mixed with 1:100 w/w fluorescein isothiocyanate (FITC)-alginate (Creative PEGWorks) to improve the distinction between core and shell for image analysis.

The CSCs were fabricated with COSMIC, a bioprinter with an aluminum stand (height = 47 cm, width = 25 cm) housing two stepper motors that actuate two syringes connected to a coaxial needle. In this study, we used two commercial coaxial needles (Ramé-hart Instrument Co., USA): needle 1 with an inner diameter = 26 Gauge (0.254 mm) and an outer diameter = 19 Gauge (0.69 mm), and needle 2 with the same inner diameter and an outer diameter = 16 Gauge (1.19 mm). Support elements for motors, syringes, and needle were printed in acrylonitrile butadiene styrene (Stratasys Fortus 250mc, USA). A 0.1 M calcium chloride bath was placed at a fixed distance (30 cm)

underneath the needle to enable alginate drop formation and crosslinking.

The extrusion flow rate was controlled via a graphical user interface (GUI) implemented in Processing (Processing Foundation, USA). Air flow can be also applied to the needle extremities through purposely designed air channels (see **Section S7** in Supplementary File for more details).

We first investigated CSC geometry as a function of the different core–shell extrusion flow rate combinations defined in the *in silico* models (10, 20, and 40 μL/s). Brightfield and fluorescence imaging (Olympus, Japan) and analysis (ImageJ) were used to trace the outer core and shell boundaries, to quantify the radii, the roundness (the ratio between the area A and the major axes a of the core and the shell boundaries, Equation VII), and the centroid coordinates, and to derive the shell thickness (difference between the shell and core radii) and the decentration of the core (distance between the shell and core centroids, an indicator of core–shell symmetry). Data were acquired in triplicate for each working condition, and statistical analysis was performed using two-way analysis of variance (ANOVA) and multiple comparison tests ($p < 0.05$).

$$\text{Roundness}\left[\%\right] = \frac{4A}{\pi a^2} \times 100 \quad \text{(VII)}$$

To identify the global parameters which most affect the geometrical features, a 3-way principal component analysis (PCA) was performed by means of the ImageJ plugin "3-way PCA"[33]. To perform the PCA analysis, the global experimental dataset was organized in a 3D matrix in which the columns represent the core and shell roundness and radii, while the rows were rearranged according to the parameter considered on the z axis, i.e., (i) the core material, (ii) the core extrusion flow rate, (iii) the shell extrusion flow rate, and (iv) the needle dimension. In all cases, the principal components identified from the plots corresponded to the core radius and its roundness.

Finally, the experimental dataset was compared with the computational data to assess the predictive power of the *in silico* tool and to optimize the model parameters through least-square minimization.

2.3. Cell encapsulation

To validate the models and generate a proof-of-concept multilayer barrier structure, we bioprinted core–shell constructs with alveolar epithelial cells in the core and fibroblasts in the shell, hereinafter referred to as Core Shell Construct 2 (CSC2). A simpler model, Core Shell Construct 1 (CSC1) with only A549 in the core, was also fabricated as control (Figure 2B). Based on the materials used, a subset of extrusion parameters was selected from the working conditions defined in the computational models. Moreover, gelatin was added to the alginate to improve cell adhesion.

For CSC2, a 20 mg/mL alginate and 20 mg/mL gelatin solution with 6 million/mL of CCD-18Co (human fibroblasts, ATCC) suspended in fetal bovine serum (FBS, F9665 Sigma Aldrich) was used to form the shell, while the core was composed of 5 million/mL A549 (alveolar epithelial cell line, ATCC) suspended in 10 mg/mL Pluronic F127 (P2443 Sigma Aldrich, Germany) prepared in complete Dulbecco's Modified Eagle Medium (DMEM, Thermo Fisher). Core and shell extrusion flow rates were respectively set at 20 and 40 μL/s, and crosslinking time at 15 min. Then, the CSCs were transferred into a 96-well culture plate (2 per well) and covered with 300 μL of transglutaminase enzyme (mTG) solution (100 U/g in complete DMEM) for 24 h to crosslink the gelatin. The mTG solution was replaced with fresh complete DMEM. For the simpler model, CSC1 with A549 in the core, the compositions were identical except that the shell material did not contain cells. Monolayer controls were prepared by seeding A549 (2×10^5 cell/cm^2) cells—M1, and CCD-18 cells (4×10^5 cell/cm^2)—M2, in Transwell ® (Corning) systems.

Cell viability was tested with the Alamar Blue assay (Sigma Aldrich) after 3 and 7 days and was calculated as a percentage of the respective monolayer controls at day 3, i.e., V_i [%] = (CSCi/Mi) × 100 (with i = 1 or 2, i.e., CSC1/M1 and CSC2/M2), and normalized for the encapsulated cell number after the bioprinting process in each type of CSC. Cell function was also evaluated in terms of (i) paracellular transport by quantifying the passage of FITC-labeled dextran (500 kDa, Sigma Aldrich)[34] and (ii) transcellular transport by analyzing the active transport of rhodamine 123 (Rho-123, Sigma Aldrich) promoted by P-glycoprotein, which is a protein expressed in the apical membrane by polarized cells[35]. Briefly, the FITC-dextran (5 mg/mL in PBS) and Rho-123 (10 μM in HBSS) solutions were poured into each well. Here, the solution external to the construct represents the basal compartment (blood side), while its core represents the apical compartment (internal lumen). After 2 h of incubation, fluorescence images of the constructs were acquired (Olympus, Japan). The amount of FITC-dextran and Rho-123 in the core was quantified by comparing pixel fluorescence intensity with known concentrations of FITC-dextran and Rho-123, respectively (using ImageJ). Passage data were normalized with respect to CSCs without cells (referred to as blanks): P [%] = (CSCi/BLANK) × 100. Data were acquired in triplet, and statistical analysis was performed using two-way ANOVA and multiple comparison tests ($p < 0.05$).

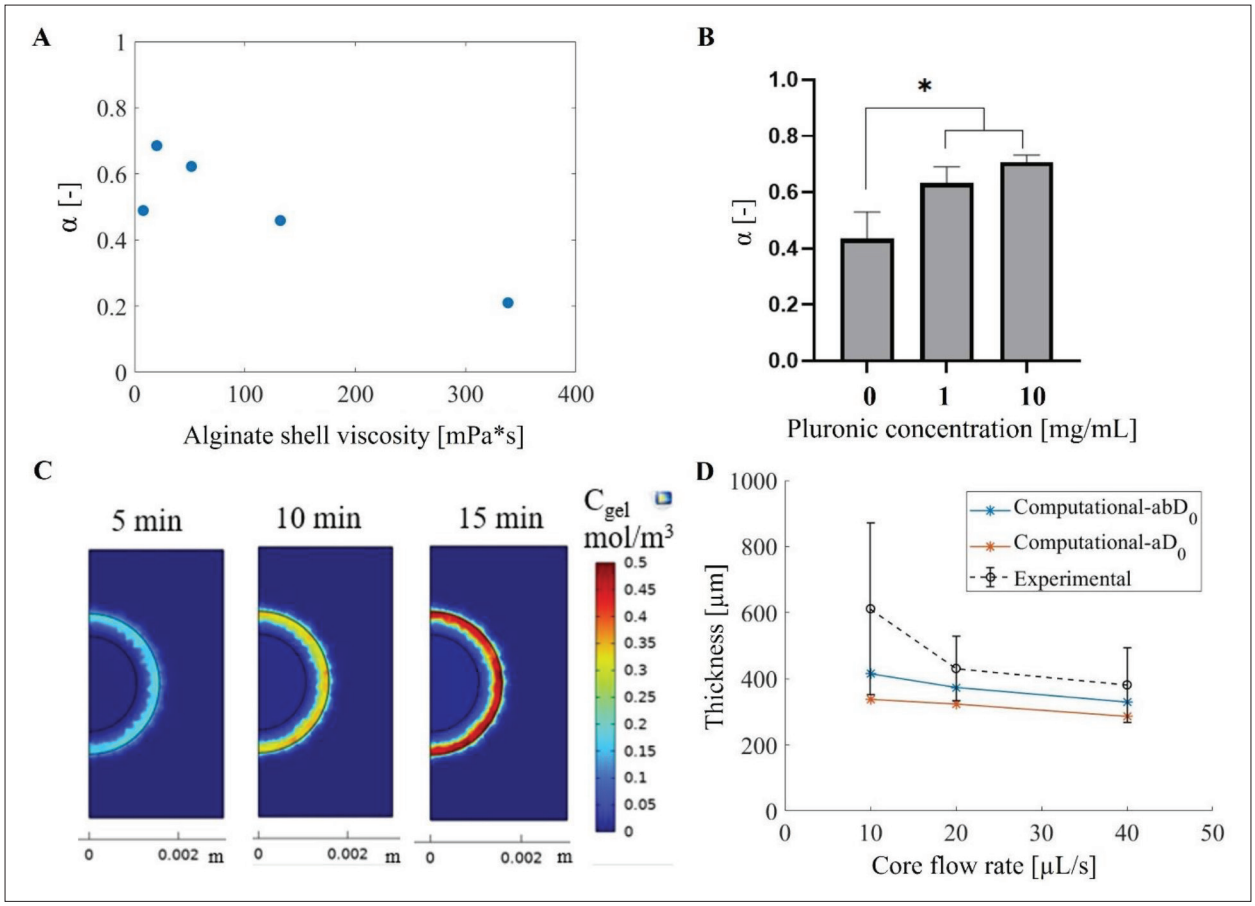

Figure 3. *In silico* results. (A) Predicted average degree of gelation (α) as a function of shell alginate viscosity (for 1 mg/mL Pluronic in the core) after 15 min in Ca^{2+} medium crosslinking. (B) Predicted average α as a function of core Pluronic concentration after 15 min in Ca^{2+} crosslinking (*$p < 0.05$). (C) Computational simulation of alginate shell formation as a function of crosslinking time (for 20 mg/mL alginate in the shell and 1 mg/mL Pluronic in the core). (D) Comparison of experimental shell thickness (black dotted line) and computational values, for the same condition in C, estimated with (blue line) and without (orange line) accounting for the Brinkman coefficient b.

3. Results

3.1. *In silico* results

The reaction diffusion models show that the degree of gelation in the shell (α) increases as a function of alginate viscosity (and hence concentration), up to a viscosity corresponding to that of 20 mg/mL alginate. After this point, α decreases with increasing alginate viscosity because Ca^{2+} ion diffusion is inhibited[36] (Figure 3A). Moreover, Figure 3B shows that the presence of Pluronic in the core significantly increases α (0.63 ± 0.06 for 1 mg/mL Pluronic, 0.71 ± 0.03 for 10 mg/mL Pluronic) with respect to a water core (0.4 ± 0.03, $p < 0.05$). However, no significant differences in the degree of gelation were observed between the two Pluronic concentrations investigated. A crosslinking degree of α = 0.6 corresponding to complete alginate gelation at the end of the crosslinking kinetics in the alginate shell occurred within 15 min in all the conditions[30,31]. Thus, this time was selected as optimal crosslinking time for all the experiments. As an example, for the condition shown in Figure 3C, the average alginate concentration in the shell (C_{gel}) = 0.47 mol/m^3, corresponding to α = 0.68 (see **Section S5** in Supplementary File).

In addition, our computations showed that after 15 min under the crosslinking process, the Ca^{2+} diffusion time within the alginate network is lower than that of un-crosslinked alginate and Pluronic (see **Section S3** and **Table S5** in Supplementary File). This suggests that alginate crosslinking occurs before core and shell material become a continuum and thus the bead structure is conserved.

Finally, Figure 3D shows that the shell thicknesses estimated considering the hindered diffusion were more similar to the experimental data with respect to the computational data derived without considering Brinkmann's coefficient *b*. This demonstrates that the

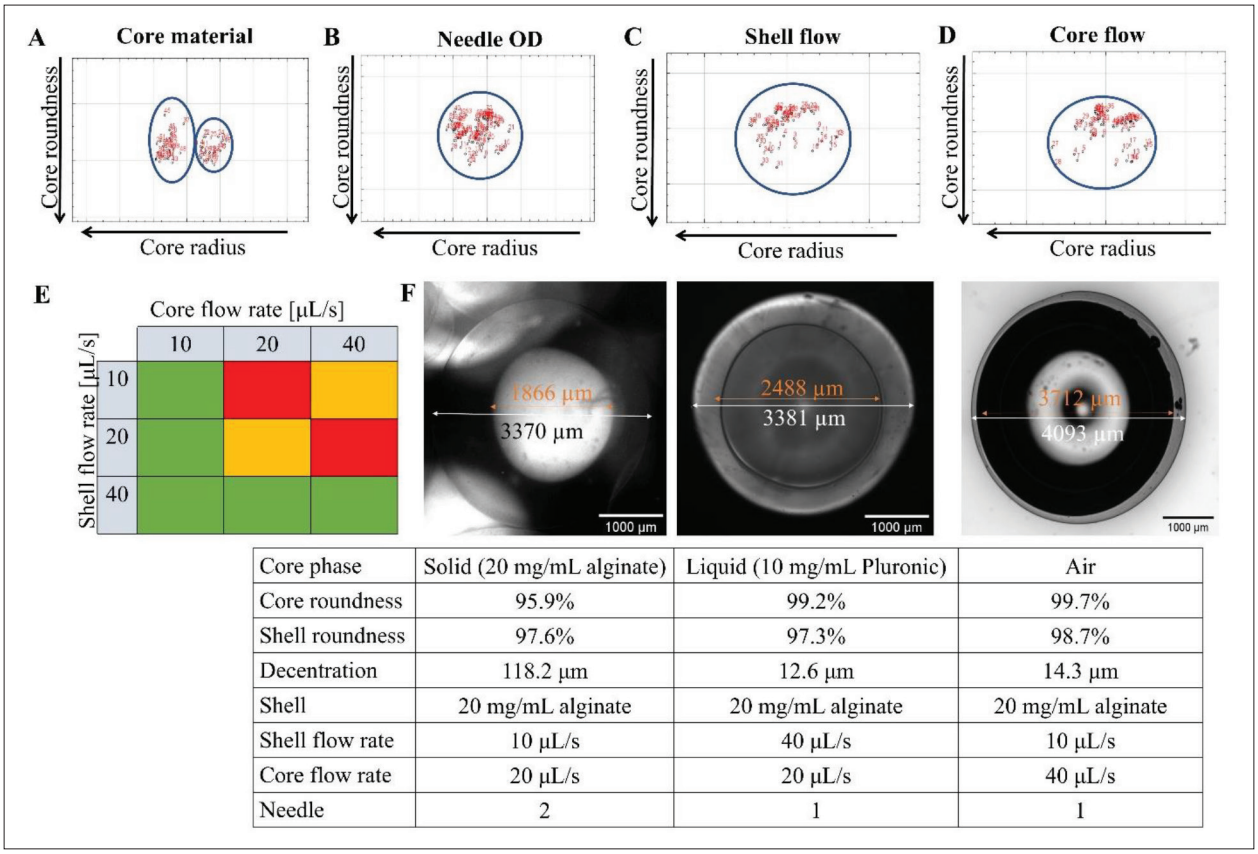

Core phase	Solid (20 mg/mL alginate)	Liquid (10 mg/mL Pluronic)	Air
Core roundness	95.9%	99.2%	99.7%
Shell roundness	97.6%	97.3%	98.7%
Decentration	118.2 μm	12.6 μm	14.3 μm
Shell	20 mg/mL alginate	20 mg/mL alginate	20 mg/mL alginate
Shell flow rate	10 μL/s	40 μL/s	10 μL/s
Core flow rate	20 μL/s	20 μL/s	40 μL/s
Needle	2	1	1

Figure 4. Experimental results. Three-way principal component analysis (PCA) results show the principal components (core radius and core roundness) for the dataset *z* axis expressed as (A) core materials, (B) needle OD, (C) shell, and (D) core extrusion flow rates. (E) Shell roundness color map for different core and shell velocity combinations (green: roundness over 90%; yellow: roundness 80%–90%; red: roundness below 80%) in the case of 10 mg/mL Pluronic core—20 mg/mL alginate shell structures. (F) Core–shell structures optimal working parameter combinations and corresponding fluorescence images for different core phases.

definition of D_{app} proposed in this work improves the predictive power of the model with respect to other models commonly used in the literature to describe alginate crosslinking[30,31].

3.2. Experimental results

For liquid and solid cores, the PCA results indicate that the parameter that most affects the CSCs is the core material (Figure 4A). Clustering was not observed for different needle ODs or shell extrusion flow rates (Figure 4B and C), indicating that they play a minor role in determining the geometrical characteristics of the CSCs. Although the PCA did not reveal any obvious clustering phenomena with respect to core flow rate (Figure 4D), the statistical analysis (*t*-test, $p < 0.05$) carried out on subgroups of data showed that this parameter strongly influences the quality (i.e., roundness) of the droplet (Figure 4E). In particular, the experimental characterization suggested that for optimal results in terms of overall roundness of the bioprinted structures, the shell extrusion flow rate should be higher than that of the core (Figure 4E).

In all the conditions investigated, the experimental results were coherent with those from the *in silico* models, thus confirming their validity (**Sections S5** and **S6** in Supplementary File report further details on the comparison between *in silico* and experimental data).

The fabrication of air-containing structures was more challenging: air encapsulation occurred only with the use of 20 mg/mL alginate and using: (i) needle 1, core flow rate of 40 μL/s, shell flow rate of 10–20 μL/s; (ii) needle 2, core flow rate of 10 μL/s and shell flow rate of 10–20 μL/s. The air-core condition was excluded from the PCA analysis due to the difficulty in obtaining air encapsulation in almost all the working conditions analyzed, which prevented the correct implementation of 3-way PCA algorithm. The optimal results in terms of roundness and core–shell symmetry for the fabrication of solid-, liquid- and air-core structures are summarized in Figure 4F. **Sections S7** and **S8** in Supplementary File report other experimental conditions investigated, i.e., the extrusion in the presence of an external air flow and the use of Pluronic in the shell.

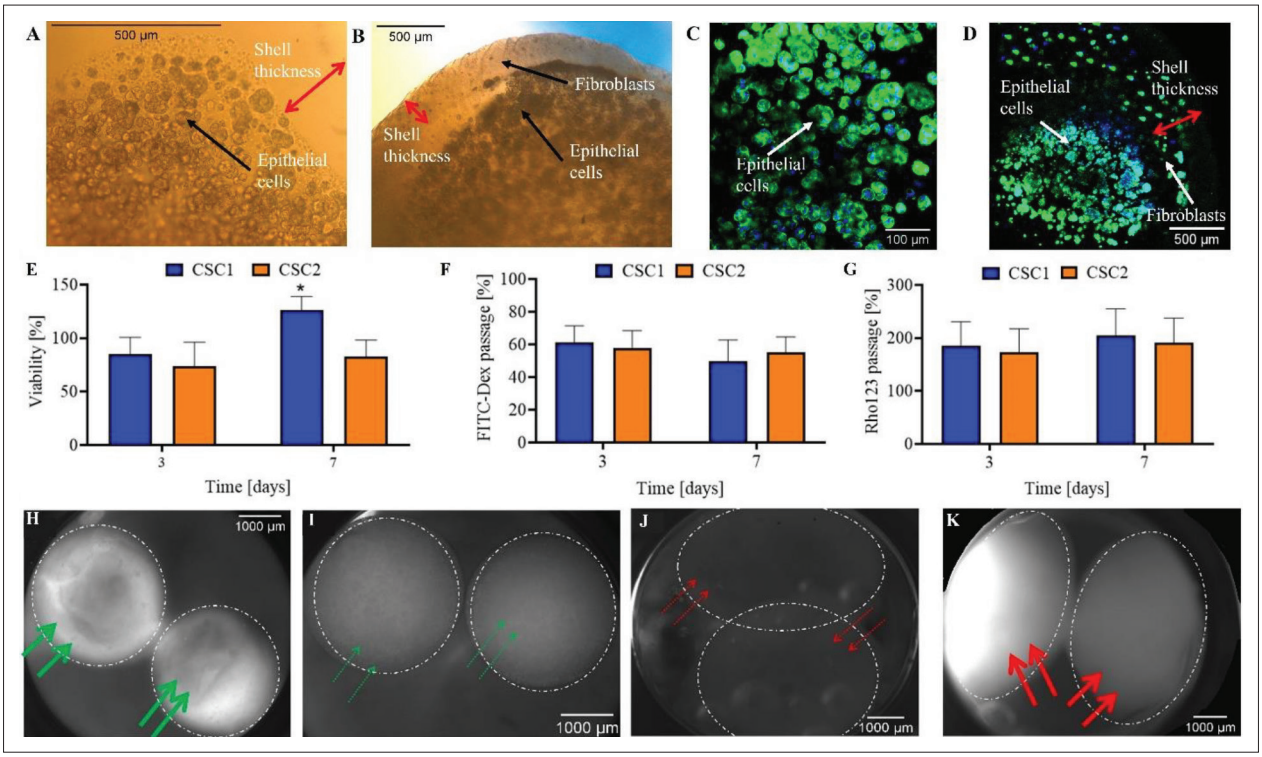

Figure 5. Cell culture. Brightfield and confocal images of CSC1 (A, C) and CSC2 (B, D) acquired at day 7; (E) CSC1 and CSC2 cell viability normalized respectively to M1 and M2 monolayer controls. (F) Paracellular (FITC-Dextran) and (G) Transcellular passage (Rho-123) normalized with respect to blanks (* $p < 0.05$). Example of fluorescence images used for deriving dextran and rhodamine passage at day 7 in CSC2 constructs (I, K) and blanks (H, J). White dotted circles highlight the constructs, while green and red arrows indicate the direction and extent of FITC-dextran and Rho-123 passage, respectively.

3.3. Evaluation of core–shell spheroids

As shown in Figure 5A–D, epithelial cells extruded in the core spontaneously adhered at the core–shell interface, while fibroblasts were homogenously distributed in the shell matrix. The viability of the encapsulated cells (Figure 5E) was slightly lower than controls at day 3 (85.18% ± 15.59% and 74.12% ± 22.07%, respectively, for CSC1 and CSC2). At day 7, the viability of CSC1 increased with respect to the previous time point, while in the case of CSC2, viability was comparable with day 3. As demonstrated by the low Thiele number (S10), higher oxygen availability is likely responsible for the observed increase in CSC1 viability. We also observed a reduction in dextran passage (Figure 5F and I) and an increase in Rho-123 transport (Figure 5G and K) with respect to blanks (Figure 5H and J) throughout the culture period for both CSC1 and CSC2. After a week, the passive passage of dextran decreased in the presence of the cells (by 50% ± 13% for CSC1 and 55% ± 10% for CSC2), while the active passage of Rho-123 increased by 204% ± 51% and 191% ± 47%, respectively, for CSC1 and CSC2. Figure 5H–K shows typical images of the constructs during passage tests.

4. Discussion

In this paper, we describe an integrated *in silico–in vitro* approach for the generation of reproducible core–shell constructs with different core phases. Our results show that the main factors affecting their fabrication are related to material properties and to the combination of core and shell extrusion speeds.

The *in silico* models allowed for the definition of the optimal experimental working window considering different material properties and extrusion parameters. In particular, the predictivity of the *in silico* model was improved by introducing a new definition of the apparent diffusion coefficient, including both the effect of gelation degree over time[30,31] and of hindered ion diffusion[32]. The FEM model showed that the formation of the core–shell structures is dependent on the fact that calcium diffusion occurs over shorter times with respect to alginate diffusion, thus preventing material mixing and allowing the formation of a layered 3D structure. Moreover, in the absence of Pluronic in the liquid core (Figure 3B), the computed gelation degree of the shell was

lower than the $\alpha = 0.6$ threshold, while it increased with increasing Pluronic concentration. Experimental tests confirmed that the presence of Pluronic was essential in the formation of the liquid-core structures. Pluronic is a copolymer of hydrophilic and hydrophobic groups which, at the concentrations employed here, forms micellar structures in aqueous solutions; hence, the entanglement between alginate or Pluronic chains can be neglected[37]. The steric hindrance and increased core viscosity offered by the micelles likely hamper alginate diffusion into the liquid core.

The experimental results also highlighted that the relative core–shell extrusion flow rate is fundamental for bioprinting core–shell structures with optimal roundness. For solid and liquid cores, the shell extrusion rate should be higher than that of the core, promoting the formation of a uniform shell layer. Although challenging, with some of these flow rate combinations, we also achieved the formation of an air-core. To the best of our knowledge, the spontaneous formation of an air-containing lumen has never been observed in bioprinted structures. This result is thus particularly relevant for lung models.

Our preliminary cellular studies demonstrated the cytocompatibility of the bioprinting process and the feasibility of encapsulating different cell types in a core–shell construct. The alveolar microenvironment was effectively recapitulated, with epithelial cells lining the lumen and fibroblasts in the shell, representing interstitial spaces in the lung extracellular matrix. In terms of architecture, the epithelial cells are exposed to a radius of curvature = 1.01 ± 0.12 mm, while fibroblasts perceive a radius of curvature which varies with their position in the shell, ranging from 1.5 ± 0.11 mm to 1.01 ± 0.12 mm. With an elastic modulus in the kPa range (see **Section S9** in Supplementary File), these constructs are also able to mimic healthy matrix conditions, thus maintaining fibroblasts in a quiescent state without the onset of fibrotic processes[38]. The reduction of FITC-dextran passage with respect to the cell-free blanks suggests that the presence of cells hindered passive diffusion, which may be linked to the onset of barrier formation. The increase of rhodamine passage with respect to the blanks is particularly interesting since it indicates active transcellular transport and epithelial cell polarization. Further studies may improve uniformity of the epithelial layer along all the lumen (e.g., by improving the composition and porosity of the shell matrix and by implementing an air–liquid interface thanks to air-filled cores fabrication). The presence of fibroblasts does not significantly affect the parameters investigated. However, since fibroblasts are fundamental for lung tissue homeostasis, in future studies, the co-culture model could be used for recapitulating other pathophysiological conditions, such as lung fibrosis and aging, by appropriately tuning material parameters (e.g., viscosity, stiffness)[38-41]. The strategy could also be exploited to generate stratified structures, such as tumors and embryonic layers[42,43], or more advanced systems mimicking the curved topology of interfaces between tissues occurring in different organs in the human body[42,44,45]. Finally, more in-depth cell studies to better understand cell response to curvature could be conducted by tuning the extrusion parameters highlighted in this work to modulate core–shell radii[41,42].

5. Conclusion

An innovative *in silico–in vitro* strategy was developed for bioprinting-structured spheroids able to replicate the multilayer tissue organization and the interface between epithelial (or endothelial) tissues and fluid (either liquid or air) lumens. The computational tools enable the definition of a working window, optimizing material combination and extrusion parameters. The generation of core–shell spheroids with our bioprinting set-up presents a significant advantage with respect to standard culture methods allowing the rapid fabrication of complex and physiologically relevant architectures. Our results show improved barrier properties with respect to controls, contributing to the establishment of human-relevant *in vitro* models, in line with 3Rs principles (refinement, reduction, and replacement of animal experiments).

Acknowledgments

None.

Funding

This research received funding from the Italian Ministry of Health for the definition alternatives to animal-based research.

Conflict of interest

The authors declare no conflicts of interest.

Author contributions

Conceptualization: Ludovica Cacopardo, Arti Ahluwalia
Investigation: Nicole Guazzelli, Ludovica Cacopardo
Methodology: Nicole Guazzelli, Ludovica Cacopardo, Alessandro Corti, Arti Ahluwalia
Formal analysis: Nicole Guazzelli, Ludovica Cacopardo
Writing – original draft: Nicole Guazzelli, Ludovica Cacopardo, Arti Ahluwalia
Writing – review: Nicole Guazzelli, Ludovica Cacopardo, Alessandro Corti, Arti Ahluwalia

Ethics approval and consent to participate

Not applicable.

Consent for publication

Not applicable.

Availability of data

Data will be available from corresponding authors upon reasonable requests.

Further disclosure

Parts of the findings have been presented in the 27th congress of the European Society of Biomechanics (Porto, Portugal), the 2022 European Congress on Alternatives to Animal Testing (EUSAAT, Linz, Austria), in the XI Annual Meeting of the ESB-ITA (Massa, Italy). Moreover, they have been included in the Proceedings of the 3rd Centro 3R annual meeting (N. Guazzelli, L. Cacopardo, and A. Ahluwalia, Biomed Sci Eng, vol. 5, no. s1, Sep. 2021).

References

1. Gómez-Gálvez P, Anbari S, Escudero LM, *et al.*, 2021, Mechanics and self-organization in tissue development. *Semin Cell Dev Biol,* 120: 147–159.

   https://doi.org/10.1016/j.semcdb.2021.07.003

2. Moysidou CM, Barberio C, Owens RM, 2021, Advances in engineering human tissue models. *Front Bioeng Biotechnol,* 8: 620962.

   https://doi.org/10.3389/fbioe.2020.620962

3. Nossa R, Costa J, Cacopardo L, *et al.*, 2021, Breathing in vitro: Designs and applications of engineered lung models. *J Tissue Eng,* 12: 1–28.

   https://doi.org/10.1177/20417314211008696

4. Cacopardo L, Costa J, Giusti S, *et al.*, 2019, Real-time cellular impedance monitoring and imaging of biological barriers in a dual-flow membrane bioreactor. *Biosens Bioelectron,* 140: 111340.

   https://doi.org/10.1016/j.bios.2019.111340

5. Costa J, Ahluwalia A, 2019, Advances and current challenges in intestinal in vitro model engineering: A digest. *Front Bioeng Biotechnol,* 7: 144.

   https://doi.org/10.3389/fbioe.2019.00144

6. de Melo BAG, Benincasa JC, Cruz EM, *et al.*, 2021, 3D culture models to study SARS-CoV-2 infectivity and antiviral candidates: From spheroids to bioprinting. *Biomed J,* 44(1): 31–42.

   https://doi.org/10.1016/j.bj.2020.11.009

7. Callens SJP, Uyttendaele RJC, Fratila-Apachitei LE, *et al.*, 2020, Substrate curvature as a cue to guide spatiotemporal cell and tissue organization. *Biomaterials,* 232: 119739.

   https://doi.org/10.1016/j.biomaterials.2019.119739

8. Arumugasaamy N, Navarro J, Kent Leach J, *et al.*, 2019, In vitro models for studying transport across epithelial tissue barriers. *Ann Biomed Eng,* 47(1): 1–21.

   https://doi.org/10.1007/s10439-018-02124-w

9. Charwat V, Egger D, 2018, The third dimension in cell culture: From 2D to 3D culture formats, in *Cell Culture Technology. Learning Materials in Biosciences,* Springer, Cham, 75–90.

   https://doi.org/10.1007/978-3-319-74854-2_5

10. Harmand N, Hénon S, 2020, 3D shape of epithelial cells on curved substrates. *Phys Rev X,* 11(3): 031028(17).

    https://doi.org/10.1103/PhysRevX.11.031028

11. Rosellini A, Freer G, Quaranta P, *et al.*, 2019, Enhanced in vitro virus expression using 3-dimensional cell culture spheroids for infection. *J Virol Methods,* 265: 99–104.

    https://doi.org/10.1016/j.jviromet.2018.12.017

12. Lee JL, Streuli CH, 2014, Integrins and epithelial cell polarity. *J Cell Sci,* 127(25): 3217–3225.

    https://doi.org/10.1242/jcs.146142

13. Samy KE, Levy ES, Phong K, *et al.*, 2019, Human intestinal spheroids cultured using sacrificial micromolding as a model system for studying drug transport. *Sci Rep,* 9(1): 1–12.

    https://doi.org/10.1038/s41598-019-46408-0

14. Abdul L, Rajasekar S, Lin DSY, *et al.*, 2020, Deep-LUMEN assay-human lung epithelial spheroid classification from brightfield images using deep learning. *Lab Chip,* 20(24): 4623–4631.

    https://doi.org/10.1039/D0LC01010C

15. Mithal A, Capilla A, Heinze D, *et al.*, 2020, Generation of mesenchyme free intestinal organoids from human induced pluripotent stem cells. *Nat Commun,* 11(1): 215.

    https://doi.org/10.1038/s41467-019-13916-6

16. Lu T, Cao Y, Zhao P, *et al.*, 2021, Organoid: A powerful tool to study lung regeneration and disease. *Cell Regeneration,* 10(1): 1–10.

    https://doi.org/10.1186/s13619-021-00082-8

17. Laselva O, Conese M, 2021, Three-dimensional airway spheroids and organoids for cystic fibrosis research. *J Respir*, 1(4): 229–247.

    https://doi.org/10.3390/jor1040022

18. Mollaki V, 2021, Ethical challenges in organoid use. *BioTech,* 10(13): 12.

    https://doi.org/10.3390/biotech10030012

19. Garreta E, Kamm RD, Chuva de Sousa Lopes SM, *et al.*, 2021, Rethinking organoid technology through bioengineering. *Nat Mater,* 20(2): 145–155.

https://doi.org/10.1038/s41563-020-00804-4

20. Fabbri R, Cacopardo L, Ahluwalia A, *et al.*, 2023, Advanced 3D models of human brain tissue using neural cell lines: State-of-the-art and future prospects. *Cells,* 12(8): 1181.

https://doi.org/10.3390/cells12081181

21. Mobaraki M, Ghaffari M, Yazdanpanah A, *et al.*, 2020, Bioinks and bioprinting: A focused review. *Bioprinting,* 18: e00080.

https://doi.org/10.1016/j.bprint.2020.e00080

22. Ahmad Raus R, Wan Nawawi WMF, Nasaruddin RR, 2021, Alginate and alginate composites for biomedical applications. *Asian J Pharm Sci,* 16(3): 280–306.

https://doi.org/10.1016/j.ajps.2020.10.001

23. Choi DH, Park CH, Kim IH, *et al.*, 2010, Fabrication of core-shell microcapsules using PLGA and alginate for dual growth factor delivery system. *J Control Release,* 147(2): 193–201.

https://doi.org/10.1016/j.jconrel.2010.07.103

24. Duarte ARC, Mano F, Reis RL, *et al.*, 2014, Microfluidic production of per fluorocarbon-alginate core – shell microparticles for ultrasound therapeutic applications. *Langmuir,* 30(41): 12391–99.

https://doi.org/10.1021/la502822v

25. Yu L, Sun Q, Hui Y, *et al.*, 2019, Microfluidic formation of core-shell alginate microparticles for protein encapsulation and controlled release. *J Colloid Interface Sci,* 539: 497–503.

https://doi.org/10.1016/j.jcis.2018.12.075

26. Kamperman T, Trikalitis VD, Karperien M, *et al.*, 2018, Ultrahigh-throughput production of monodisperse and multifunctional janus microparticles using in-air microfluidics. *ACS Appl Mater Interfaces,* 10(28): 23433–23438.

https://doi.org/10.1021/acsami.8b05227

27. Agarwal P, Choi JK, Huang H, *et al.*, 2015, A biomimetic core-shell platform for miniaturized 3D cell and tissue engineering. *Part Part Syst Charact,* 32(8): 809–816.

https://doi.org/10.1002/ppsc.201500025

28. Wang H, Liu H, Liu H, *et al.*, 2019, One-step generation of core–shell gelatin methacrylate (GelMA) microgels using a droplet microfluidic system. *Adv Mater Technol,* 4(6): 1–10.

https://doi.org/10.1002/admt.201800632.

29. Wilkes ED, Phillips SD, Basaran OA, 1999, Computational and experimental analysis of dynamics of drop formation. *Phys Fluids,* 11(12): 3577–3598.

https://doi.org/10.1063/1.870224

30. Hajikhani A, Wriggers P, Marino M, 2021, Chemo-mechanical modelling of swelling and crosslinking reaction kinetics in alginate hydrogels: A novel theory and its numerical implementation. *J Mech Phys Solids,* 153: 104476.

https://doi.org/10.1016/j.jmps.2021.104476

31. Hajikhani A, Scocozza F, Conti M, *et al.*, 2019, Experimental characterization and computational modeling of hydrogel cross-linking for bioprinting applications. *Int J Artif Organs,* 42(10): 548–557.

https://doi.org/10.1177/0391398819856024

32. Pluen A, Netti PA, Jain RK, *et al.*, 1999, Diffusion of macromolecules in agarose gels: Comparison of linear and globular configurations. *Biophys J,* 77(1): 542–552.

https://doi.org/10.1016/S0006-3495(99)76911-0

33. Tirella A, Magliaro C, Penta M, *et al.*, 2014, Sphyga: A multiparameter open source tool for fabricating smart and tunable hydrogel microbeads. *Biofabrication,* 6(2): 025009. DOI 10.1088/1758-5082/6/2/025009

https://doi.org/10.1088/1758-5082/6/2/025009

34. Frost TS, Jiang L, Lynch RM, *et al.*, 2019, Permeability of epithelial/endothelial barriers in transwells and microfluidic bilayer devices. *Micromachines (Basel),* 10(8): 8:553.

https://doi.org/10.3390/mi10080533

35. Costa J, Almonti V, Cacopardo L, *et al.*, 2020, Investigating curcumin/intestinal epithelium interaction in a millifluidic bioreactor. *Bioengineering,* 7(3): 100.

https://doi.org/10.3390/bioengineering7030100

36. Matricardi P, Pontoriero M, Coviello T, *et al.*, 2008, In situ cross-linkable novel alginate-dextran methacrylate IPN hydrogels for biomedical applications: Mechanical characterization and drug delivery properties. *Biomacromolecules,* 9(7): 2014–2020.

https://doi.org/10.1021/bm800252c

37. Bharatiya B, Ghosh G, Aswal VK, *et al.*, 2010, Effect of n-Hexanol and n-Hexylamine on the micellar solutions of pluronic F127 and P123 in water and 1M NaCl. *J Dispers Sci Technol,* 31(5): 660–667, DOI: 10.1080/01932690903212867

http://dx.doi.org/10.1080/01932690903212867

38. White ES, 2015, Lung extracellular matrix and fibroblast function. *Ann Am Thorac Soc,* 12(1): 30–33.

https://doi.org/10.1513/AnnalsATS.201406-240MG

39. Ushakumary MG, Riccetti M, Perl AKT, 2021, Resident interstitial lung fibroblasts and their role in alveolar stem cell niche development, homeostasis, injury, and regeneration. *Stem Cells Transl Med,* 10(7): 1021–1032.

https://doi.org/10.1002/sctm.20-0526

40. Cacopardo L, Ahluwalia A, 2021, Engineering and monitoring 3D cell constructs with time-evolving viscoelasticity for the study of liver fibrosis in vitro. *Bioengineering,* 8(8): 106.

https://doi.org/10.3390/bioengineering8080106

41. Cacopardo L, Guazzelli N, Ahluwalia A, 2022, Characterizing and engineering biomimetic materials for viscoelastic mechanotransduction studies. *Tissue Eng Part B Rev,* 28(4): 912–925.

https://doi.org/10.1089/ten.teb.2021.0151

42. Mastrorocco A, Cacopardo L, Lamanna D, *et al.*, 2021, Bioengineering approaches to improve in vitro performance of prepubertal lamb oocytes. *Cells,* 10(6): 1458.

https://doi.org/10.3390/cells10061458

43. Pinto B, Henriques AC, Silva PMA, *et al.*, 2020, Three-dimensional spheroids as in vitro preclinical models for cancer research. *Pharmaceutics,* 12(12): 1–38.

https://doi.org/10.3390/pharmaceutics12121186

44. Visco V, Bava FA, D'Alessandro, F, *et al.*, 2009, Human colon fibroblasts induce differentiation and proliferation of intestinal epithelial cells through the direct paracrine action of keratinocyte growth factor. *J Cell Physiol,* 220(1): 204–213.

https://doi.org/10.1002/jcp.21752

45. Roulis M, Flavell, RA, 2016, Fibroblasts and myofibroblasts of the intestinal lamina propria in physiology and disease. *Differentiation,* 92(3): 116–131.

https://doi.org/10.1016/j.diff.2016.05.002